Effects of annealing on photoluminescence and defect interplay in ZnO bombarded by heavy ions: crucial role of the ion dose

Alexander Azarov[1,2,a)], Augustinas Galeckas[1], Cyprian Mieszczyński[2], Anders Hallén[3], and Andrej Kuznetsov[1]

[1] *University of Oslo, Department of Physics, Centre for Materials Science and Nanotechnology, PO Box 1048 Blindern, N-0316 Oslo, Norway*

[2] *NOMATEN Centre of Excellence, National Centre for Nuclear Research, A. Soltana 7, 05-400 Otwock-Świerk, Poland*

[3] *Royal Institute of Technology, KTH-EECS, Electrum 229 SE-164 40, Stockholm, Sweden*

Bombardment of ZnO with heavy ions generating dense collision cascades is of particular interest because of the formation of non-trivial damage distribution involving a defected layer located between the surface and the bulk damage regions, as seen by Rutherford backscattering spectroscopy in the channeling mode. By correlating photoluminescence and channeling data we demonstrate that the thermal evolution of defects in wurtzite ZnO single crystals implanted with Cd ions strongly depends on the implanted dose. Specifically, the ion dose has a profound effect on the optical response in the spectral range between the near-band-edge emission and deep level emission bands. The interplay between interstitial and vacancy type defects during annealing is discussed in relation to the evolution of the multipeak damage distribution.

a) alexander.azarov@smn.uio.no

I. Introduction

During the past decade research interest in ZnO and related materials has been stimulated by their outstanding properties and potential applications in optoelectronics, spintronics, for gas sensors, etc. [1]. However, insufficient understanding of defects and their effects on physical/chemical properties of the material limits the realization of ZnO-based devices. One of the most efficient methods of introducing defects in crystalline materials is by ion implantation. In general, the resulting amount of radiation defects and their depth distribution after such bombardment depend on ion mass and energy, implanted dose, sample temperature, ion flux, and crystal orientation [2]. Ion mass and energy determine the density of a collision cascade generated by an impinging ion, and often the cascade density can be considered as a separate parameter [3]. Thermal annealing is conventionally used as a post-implant treatment to remove implantation defects and, therefore, restore crystalline structure along with transferring implanted impurities into substitutional positions [4-6].

Radiation effects in ZnO have been intensively studied during the past decade [5-15]. In particular, it was demonstrated that ZnO exhibits very efficient dynamic defect annealing and, in fact, this material cannot be rendered amorphous even at ion bombardment at cryogenic temperatures [6, 8]. However, defects of various types form during ion bombardment and the kinetics of their formation and annealing strongly depends on ion species, so that dopant-defect reactions often determine the dominant defect structures after processing [9]. One of the most intriguing features of defect formation in ZnO is related to the irradiation regimes where dense collision cascades are generated. Indeed, despite that the density of collision cascades has a minor effect on the total amount of defects generated by energetic ions, the defect versus depth profile exhibits an abnormal multi-layered distribution for dense collision cascades [10]. In the present contribution, we study the formation and thermal stability of defects in ZnO

implanted with Cd ions, which are expected to produce collision cascades dense enough for the formation of a multi-layered damage distribution.

II. Experimental

Wurtzite ZnO single crystals were implanted at room temperature by 250 keV $^{112}Cd^{+}$ ions with low (5×10^{14} cm^{-2}) and high (5×10^{15} cm^{-2}) ion doses. The implantations were carried out at 7° off the [0001] direction in order to reduce channeling. After implantation, the samples were annealed at temperatures in the range of 600-1000 °C for 30 min in air using a conventional tube furnace. The ion-induced structural disorder before and after anneals was analyzed by Rutherford backscattering spectrometry in the channeling mode (RBS/C) with 2.0 MeV $^{4}He^{+}$ ions backscattered into a detector placed at 100° relative to the incident beam direction. This so-called glancing-angle detector geometry was used to provide enhanced depth resolution, specifically in the near-surface region where a multi-layered damage distribution is expected to form.

Analysis of raw RBS/C spectra was performed using the McChasy simulation code [11]. Note that the codes typically used for the analysis of RBS/C spectra allow estimating the number of displaced atoms as a function of depth only under the assumption of uncorrelated defect structures. This assumption provides reliable results only if the disordered region consists of simple defects, such as point defects and/or point defect clusters. However, ion bombardment often leads to the formation of extended defects, such as stacking faults and/or dislocation loops, in addition to the simple defects. The scattering mechanism of the analyzing beam is different for point and extended defects, and analysis of RBS/C spectra under the above mentioned assumption typically leads to an overestimation of the number of displaced atoms and gives rise to unphysical artefacts, such as deep tails in the defect depth profiles, if many

extended defects are present. In contrast, McChasy code simulations allow separating contributions from randomly displaced atoms (RDA) and extended defects (DIS), thus, making it possible to analyze formation and evolution of defects of different types. However, it should be kept in mind that the relative contribution to the backscattering is different for the extended defects lying in different crystallographic planes. Thus, for the channeling analysis performed along [0001] direction, extended defects along the basal plane give rise to a backscattering signal similar to that of RDA defects [7]. Therefore, in the McChasy simulations the DIS defects represent only extended defects which are perpendicular to the sample surface, e.g. dislocation loops lying in prismatic planes, while defects such as basal plane stacking faults, are included in RDA.

Optical properties of the samples were studied by photoluminescence (PL) measurements carried out at 10 K and using a 325 nm wavelength cw-HeCd laser as an excitation source. The emission was analyzed by an imaging spectrometer system (Horiba iHR320 coupled to Andor LM658M EMCCD) with a spectral resolution below 2 nm.

III. Results and discussion

A. RBS/C results

The evolution of ion beam induced disorder in ZnO in the course of post-implant thermal treatments is illustrated in Fig. 1, showing RBS/C spectra of the samples implanted with low (5×10^{14} cm^{-2}) and high (5×10^{15} cm^{-2}) doses of Cd ions before and after anneals, as indicated in the legends. For both doses, a distinct multipeak damage distribution forms with an intermediate peak (labeled as IP and indicated by the arrows in both panels) located between the surface peak (SP) and the more expected damage layer (BP) in around the projected range ($R_p \approx 65$ nm according to the SRIM code [12]

simulations). For the low dose, IP is located close to the surface peak, while its depth position is close to 25 nm in the case of the high dose. Such behavior is corroborated with previous results, where it was shown that IP originates from the surface and moves into the crystal bulk with increasing ion dose until it becomes unresolvable from the bulk damage [10, 13]. The mechanism for the IP formation is not fully understood, but it has been suggested that it is related to the Zn-rich interface between the stoichiometric ZnO and the near-surface region with altered composition [15].

Remarkably, the defect annealing kinetics strongly depends on the implanted dose as can be clearly seen from Fig. 1. Indeed, annealing in the temperature range 600-800 °C has a minor effect on the bulk peak (BP) for low dose (Fig. 1(a)), however leads to the shift of the IP position towards the bulk damage and its position reaches 33 nm in depth below the surface after the 800 °C anneal. Moreover, the damage level below the IP is lower as compared to that before annealing, so that the BP is partly annealed in this region and a gap located between IP and BP formed. Such behavior may indicate that the moving IP leads to the enhanced annihilation of ion-induced defects in its vicinity. Therefore defects in IP play an important role on crystal recovery, however exact mechanism of this process is not clear and more studies are currently needed to better understand the role of IP on defect annealing kinetics in ZnO. Further annealing at higher temperature leads to dramatic removal of the defects, and RBS/C spectrum becomes very similar to that of the virgin one indicating practically complete recovery of the crystal lattice. In contrast, for high dose, Fig. 1(b), a substantial damage annealing in the region of BP occurs already at 600 °C, while position of the IP shifts to ~50 nm and it becomes partly overlapped with BP at this temperature. Annealing at higher temperatures leads to disappearance of the IP and a gradual crystal recovery, however, the channeling spectrum is still higher than that for a virgin sample even after a 1000 °C anneal. Note that the RBS/C spectra of the annealed high dose samples have a relatively

high dechanneling level in the region beyond the BP, indicating a large fraction of extended defects in the annealed samples [17, 18].

Previously, it was suggested that these extended defects can affect rapid damage annealing at relatively low temperatures, leading to a two-stage damage annealing kinetics, where point defects and small defect clusters anneal at the first stage, while extended defects require higher temperatures to completely anneal out and their concentration gradually decreases with increasing temperature [9]. The different thermal budgets required for annealing defects of different types and how the annealing depends on the implanted dose is also illustrated by simulations performed with the McChasy code. Indeed, Fig. 2(a) shows the depth profiles of randomly displaced atoms (RDA) and extended defects (DIS) obtained with McChasy code simulations for both the low and high implanted doses. Note that the simulated RBS/C spectra are in a good agreement with the experimental ones as clearly illustrated by Fig. 1, where the simulated profiles are shown by the solid lines. It might be seen from Fig. 2(a) that extended defects form mainly in the end-of-range region, while the RDA peak is located closer to the R_p of the implanted ions. It should be noted that different location of the DIS and RDA defects corroborates well with a transmission electron microscopy study of defect microstructure in N implanted ZnO, where authors observed domination of prismatic dislocation loops in the end-of-range region [19]. The thermal evolution of RDA (solid lines) and DIS (dashed lines) defects obtained from McChasy simulations in the high dose sample are shown in Fig. 2(b). It might be seen that the annealing leads to the decrease of the both type of defects; however, both RDA and DIS defects are still persist after annealing at the highest temperature used. It is important to note that although decreasing the amount of the both type of defects, annealing does not affect their localization, so that the maximum of the DIS defects is situated deeper than that of RDA after all the anneals. The thermal evolution of the different types of defects can be

further investigated by comparing temperature dependences of integral disorder and Fig. 3 shows integral RDA and DIS disorder obtained from simulations as a function of annealing temperature. In contrast to the high dose, for the low dose sample the number of both extended defects and RDA start to decrease only after annealing at >800 °C. Note that some increase of the RDA concentration after the 600 °C anneal for the low dose sample may occur due to IP which becomes completely separated from the SP at this temperature; however other mechanisms related to the defect reconstruction can play also a role. For the high dose, the amount of both the RDA and DIS defects decreases with increasing temperature in the whole temperature range used, although the extended defects anneal out more slowly as compared to RDA, supporting the conclusions made above regarding the two-stage damage annealing kinetics in the heavily damaged samples.

B. PL spectroscopy

Further insights into the defect annealing kinetics were obtained from low temperature PL spectroscopy measurements, allowing for identification and monitoring of intrinsic defects as well as recovery of crystallinity upon annealing. Figure 4 presents the evolution of the PL spectra taken at 10 K of the low dose sample after different post-implantation thermal treatments. In contrast to the unimplanted (virgin) sample, which demonstrates very intensive characteristic near-band-edge (NBE) and deep-level (DLE) emissions (see the discussion below for the peak identification in these spectral ranges), the as-implanted material demonstrates very low total luminescence yield indicating the prevalence of non-radiative recombination pathways provided by ion implantation damage. However, already after 600 °C annealing, the NBE and DLE features emerge in the PL spectra. Further annealing at higher temperatures leads to formation of yet another distinctive spectral feature located in the intermediate region between NBE and

DLE and labeled as Di in Fig. 4. One should note that the assignment of optical transitions to peaks in PL spectra of ZnO in the literature is often contradictory, and most debatable in this regard is the origin of DLE, whereas the blue-violet emission in the intermediate region Di is scarcely reported and generally lacks views on the mechanisms involved. The broad DLE band spanning the range from violet to near-infrared is actually comprised of several overlapping components, which appear most clearly distinguishable in the spectrum of as-implanted ZnO in Fig. 4. The so-called red luminescence (RL) in the 1.6-1.8 eV range is commonly associated with luminescent defect clusters involving zinc vacancies (V_{Zn}) [20, 21]. The origin of the green luminescence (GL) within the range of 2.35-2.53 eV remains controversial with several emission mechanisms proposed that involve oxygen vacancies V_O [22, 23], zinc vacancies V_{Zn} [24, 25], zinc interstitials Zn_i [26], antisites O_{Zn} [27], copper impurities [28, 29], and surface states [30]. From a theoretical perspective, the reported first-principles calculations suggest V_{Zn} as the most likely candidate for the green luminescence as it forms a deep acceptor with low formation energy [31].

The general trend in the DLE region of spectra upon annealing is apparent from the comparison of the extremes, the as-implanted versus 900 °C annealed sample. The emission is initially dominated by RL (~1.8 eV) indicating the prevalence of V_{Zn} defect clusters in the as-implanted material. This DLE component is ultimately overtaken by strong GL (2.35-2.53 eV) indicating the change of the intrinsic defect balance in favor of isolated V_{Zn} and/or Vo upon the high-temperature annealing, as well as general recovery of the crystallinity. As regards to the implantation dose of the samples, we find that spectral developments are very similar for both low and high ion dose (not shown), and note that Fig. 4 represents typical behavior of ion implanted ZnO [32].

In contrast to DLE, the thermal evolution of NBE and Di features is strongly dependent on the implanted ion dose in this dose regime. The intermediate spectral region between NBE and DLE is enlarged and analyzed in detail in Fig. 5, where a set of vertical drop lines (labeled 1-8) marks the key emission components. The PL intensities at the designated spectral positions are plotted as a function of annealing temperature in Fig. 6. Starting from the UV side of the spectra in Fig. 5, the narrow luminescence band observed near the fundamental band edge at around 3.36 eV (label 1) originates from the radiative recombination of excitons bound to impurities, such as aluminum (3.3608 eV), which is omnipresent in ZnO, and gallium (3.3598 eV) [33]. The intensity of this NBE component in Fig. 5 and Fig. 6 can be considered as a direct measure of the crystallinity that allows monitoring the recovery of implantation induced damage after different annealings.

The next two partially overlapping components (see markers 2 and 3 at 3.32 eV and 3.31 eV in Fig. 5) are excitonic in nature and could be related to two-electron satellite (TES) of the main bound-exciton and free-exciton phonon replica (FX-LO) lines, respectively. The alternative candidates in this vicinity are excitons bound to structural defects and localized acceptor states on the stacking faults with the reported line positions at 3.333 eV [1] and 3.31 eV [34], respectively. Note that these two emission components are greatly affected both by ion implantation dose and annealing temperature.

The emission component centered at 3.25 eV (label 4) is associated with donor-to-acceptor pair (DAP) transitions, and possibly also affected by manifestation of the (TES-LO) line (3.25 eV) [1].

In the violet region of the visible spectrum, the PL components at 3.16 eV (label 5) and 3.06 eV (label 7) are associated with free-to-bound transitions involving

valence/conduction bands (VB, CB) and zinc interstitials ($Zn_i \rightarrow$VB) [35, 36] and/or vacancies (CB $\rightarrow V_{Zn}$) [37, 38]). The broad band peaking at 3.11 eV (label 6) is probably a cumulative outcome (convolution) of two neighboring peaks. Note that these three emissions are strongly affected by ion dose and thermal treatment.

The last component in the intermediate region positioned at 2.9 eV (label 8) is associated with zinc related ($Zn_i \rightarrow V_{Zn}$) and possibly (CB $\rightarrow O_i$) transitions [39, 40].

C. Discussion

Thermal evolution of the key emission components can be best followed by referring to both Fig. 5 and Fig. 6, the latter allowing for direct comparison of the samples implanted with low and high ion doses as well as general trends. First, we note striking differences of the NBE features in the case of high and low dose implantation as can be seen in Figs. 5 and 6. For low dose, the NBE peak is a dominating feature in all post-annealing spectra (600-900 °C), which is indicative of low residual implantation damage. The NBE intensity reaches a maximum upon annealing at 800 °C and then decreases again upon 900 °C treatment, most likely due to competition from the massively increased GL in the overall recombination process. Although a similar trend upon annealings can be observed in the case of high dose implantation (Fig. 6(b)), considerably lower (×5 fold) intensity of the NBE peak implies certain crystallinity issues related to incomplete recovery of higher implantation damage resulting in residual non-radiative pathways. This assumption is supported by RBS/C results in Fig. 3 showing significantly higher amounts of RDA and DIS defects in the case of high dose implantation. This comes along with another major discrepancy between the high dose and low dose spectra, namely, the dominance of the two closely positioned emission components (see markers at 3.32 eV and 3.31 eV in Fig. 5), which can be

readily associated with extended structural defects, as mentioned earlier. The higher ion dose implies higher implantation induced damage, including higher densities of extended DIS defects, as indeed evidenced by the RBS results in Fig. 3. As one can see in Fig. 6(b), the emission intensity reaches maximum after annealing at 700 °C and then somewhat reduces, possibly as a result of thermal dissociation of defects, but the reduction may also be affected by thermally induced migration of defects. Indeed, there is an intricate interplay between the fixed PL probing depth (α^{-1} ~60 nm for excitation at 325 nm wavelength) and defect motion into the crystal bulk upon anneals (Fig. 1(a)). The consequence of defects escaping beyond the probed depth would be the intensity drop of certain PL peaks that could be misinterpreted as a sign of effective anneal out. The next emission component at 3.25 eV is associated with donor-to-acceptor pair (DAP) transitions and, for all annealing temperatures, demonstrates certain anti-correlation of intensity for low and high dose cases with the emission maximum also at different annealing temperatures, 800 °C and 700 °C, respectively.

From the reviewed potential candidates for the violet emission, it follows that spectral development in this region is primarily associated with Zn interstitials and vacancies. The broad band peaking at 3.11 eV is possibly a result of convolution of the two neighboring peaks at 3.16 eV and 3.06 eV (each clearly distinguishable in Fig. 5(c and d)), which are associated with zinc interstitials and vacancies, respectively. These three emissions are strongly affected by ion dose and thermal treatment, as can be observed in Figs. 5 and 6. Indeed, a strong peak centered around 3.11 eV emerges in the high dose sample and it is the dominant emission in Di region after annealing at 800 °C, while further annealing at higher temperature leads to decreasing emission in this spectral range. In contrast, in the low dose sample, the emission in this region is not so intensive; however, the 2.9 eV peak is clearly visible reaching the maximum after 800

°C anneal. Bearing in mind that the 2.9 eV peak can be associated with Zn vacancies, it can be speculated that thermally-induced movement of the IP peak (Fig. 1(a)) is accompanied by the formation of Zn vacancies. It should also be noted that formation of vacancies was put forward to explain trapping of Li atoms at IP during annealing in Er implanted ZnO single crystals [41]. The intensity of the emission peaks in the Di region starts to decrease only after annealing at 900 °C, indicating partial improvement of the crystal lattice, which is in agreement with RBS/C results.

IV Conclusions

In summary, the thermal evolution of ion-induced defects in ZnO single crystals implanted with Cd ions strongly depends on the implanted dose. Channeling analysis reveals a complex damage distribution with an intermediate peak located between the sample surface and the more expected bulk damage layer. In the case of high dose, the damage exhibits a distinct two-stage annealing behavior, while the annealing of the damage at low dose is characterized by the intermediate peak moving inwards into the crystal bulk with increasing temperature. Nearly complete crystal recovery occurs after annealing at 900 °C only for the low dose implanted samples. Temperatures in excess of 1000 °C are required in the case of the high dose samples, although the annealing is still not as complete as for the low dose case annealed at 900 °C. Furthermore, simulations performed with the McChasy code strongly support complexity of the annealing process associated with thermal stability of different type defects. Additionally, PL analysis revealed different dominant optical signatures and their evolution in the spectral region between the near-band-edge and deep level emissions for the samples implanted with high and low dose, thus further elucidating the role of extended and point defects.

Acknowledgments

This work was performed within the Research Centre for Sustainable Solar Cell Technology (FME SuSolTech, Project No. 257639), co-sponsored by the Norwegian Research Council (RCN) and research and industry partners. The authors also acknowledge RCN for the support to FUNDAMENT project (No. 251131).

References:

1. Ü. Özgür, Ya. I. Alivov, C. Liu, A. Teke, M. A. Reshchikov, S. Doğan, V. Avrutin, S.-J. Cho, and H. Morkoç, "A comprehensive review of ZnO materials and devices", J. Appl. Phys. **98**, 041301 (2005).
2. J. S. Williams, "Materials modification with ion beams", Rep. Prog. Phys. **49**, 491 (1986).
3. P. A. Karaseov, A. Yu. Azarov, A. I. Titov, and S. O. Kucheyev, "Density of displacement cascades for cluster ions: an algorithm of calculation and the influence on damage formation in ZnO and GaN", Semiconductors **43**, 691, (2009).
4. E. Sonder, R. A. Zhur, and R. E. Valiga, "Annealing of damage and stability of implanted ions in ZnO crystals", J. Appl. Phys. **64**, 1140 (1988).
5. Z. Q. Chen, M. Maekawa, A. Kawasuso, S. Sakai, and H. Naramoto, "Annealing process of ion-implantation-induced defects in ZnO: Chemical effect of the ion species", J. Appl. Phys. **99**, 093507 (2006).
6. A. Yu. Azarov, E. Wendler, A. Yu. Kuznetsov, and B. G. Svensson, "Crucial role of implanted atoms on dynamic defect annealing in ZnO", Appl. Phys. Lett. **104**, 052101 (2014).
7. A. Turos, P. Jóźwik, M. Wójcik, J. Gaca, R. Ratajczak, and A. Stonert, "Mechanism of damage buildup in ion bombarded ZnO", Acta Materialia **134**, 249 (2017).
8. K. Lorenz, E. Alves, E. Wendler, O. Bilani, W. Wesch, and M. Hayes, "Damage formation and annealing at low temperatures in ion implanted ZnO", Appl. Phys. Lett. **87**, 191904 (2005).

9. A. Yu. Azarov, A. Hallén, P. Rauwel, X. L. Du, A. Yu. Kuznetsov, and B. G. Svensson, "Effect of implanted species on thermal evolution of ion-induced defects in ZnO", J. Appl. Phys. **115**, 073512 (2014).

10. A. Yu. Azarov, S. O. Kucheyev, A. I. Titov, and P. A. Karaseov, "Effect of the density of collision cascades on ion implantation damage in ZnO", J. Appl. Phys. **102**, 083547 (2007).

11. A. Turos, P. Jozwik, L. Nowicki, N. Sathish, "Ion channeling study of defects in compound crystals using Monte Carlo simulations", Nucl. Instrum. Methods B **332**, 50 (2014).

12. J. F. Ziegler, M. D. Ziegler, and J. P. Biersack, "SRIM – The stopping and range of ions in matter (2010)", Nucl. Instrum. Methods B **268**, 1818 (2010).

13. S. O. Kucheyev, J. S. Williams, C. Jagadish, J. Zou, C. Evans, A. J. Nelson, and A. V. Hamza, "Ion-beam-produced structural defects in ZnO", Phys. Rev. B **67**, 094115 (2003).

14. M. A. Myers, M. T. Myers, M. J. General, J. H. Lee, L. Shao, and H. Wang, "P-type ZnO thin films achieved by N^+ ion implantation through dynamic annealing process", Appl. Phys. Lett. **101**, 112101 (2012).

15. M. T. Myers, S. Charnvanichborikarn, C. C. Wei, Z. P. Luo, A. Aitkaliyeva, L. Shao, and S. O. Kucheyev, "Defect microstructure in heavy-ion-bombarded (0001) ZnO", Acta Materialia **60,** 6086 (2012).

16. J. Kennedy, P. P. Murmu, E. Manikandan, and S. Y. Lee, "Investigation of structural and photoluminescence properties of gas and metal ions doped zinc oxide single crystals," J. Alloys Compd. **616**, 614 (2014).

17. A. Azarov, P. Rauwel, A. Hallén, E. Monakhov, and B. G. Svensson, "Extended defects in ZnO: Efficient sinks for point defects", Appl. Phys. Lett. **110**, 022103 (2017).

18. A. Turos, L. Nowicki, A. Stonert, K. Pagowska, J. Jagielski, and A. Muecklich, "Monte Carlo simulations of ion channeling in crystals containing extended defects", Nucl. Instrum. Methods B **268**, 1718 (2010).

19. G. Perillat-Merceroz, P. Gergaud, P. Marotel, S. Brochen, P.-H. Jouneau, and G. Feuillet, "Formation and annealing of dislocation loops induced by nitrogen implantation of ZnO", J. Appl. Phys. **109**, 023513 (2011).

20. Y. Dong, F. Tuomisto, B. G. Svensson, A. Yu. Kuznetsov, and L. J. Brillson, "Vacancy defect and defect cluster energetics in ion-implanted ZnO", Phys. Rev. B **81**, 081201 (2010).

21. K. E. Knutsen, A. Galeckas, A. Zubiaga, F. Tuomisto, G. C. Farlow, B. G. Svensson, and A. Yu. Kuznetsov, "Zinc vacancy and oxygen interstitial in ZnO revealed by sequential annealing and electron irradiation", Phys. Rev. B **86**, 121203(R) (2012).

22. K. Vanheusden, C. H. Seager, W. L. Warren, D. R. Tallant, and J. A.Voigt, "Correlation between photoluminescence and oxygen vacancies in ZnO phosphors", Appl. Phys. Lett. **68**, 403 (1996).

23. F. Leiter, H. Alves, D. Pfisterer, N. G. Romanov, D. M. Hofmann, and B. K. Meyer, "Oxygen vacancies in ZnO", Physica B **340**, 201 (2003).

24. T. M. Børseth, B. G. Svensson, and A. Yu. Kuznetsov, "Identification of oxygen and zinc vacancy optical signals in ZnO", Appl. Phys. Lett. **89**, 262112 (2006).

25. A. Janotti and C. G. V. de Walle, "Fundamentals of zinc oxide as a semiconductor", Rep. Prog. Phys. **72**, 126 501 (2009).

26. N. O. Korsunska, L. V. Borkovska, B. M. Bulakh, L. Y. Khomenkova, V. I. Kushnirenko, and I. V. Markevich, "The influence of defect drift in external electric field on green luminescence of ZnO single crystals", J. Luminescence **102**, 733 (2003).

27. B. Lin, Z. Fu, and Y. Jia, "Green luminescent center in undoped zinc oxide films deposited on silicon substrates", Appl. Phys. Lett. **79**, 943 (2001).

28. N. Y. Garces, L. Wang, L. Bai, N. C. Giles, L. E. Halliburton, and G. Cantwell, "Role of copper in the green luminescence from ZnO crystals", Appl. Phys. Lett. **81**, 622 (2002).

29. R. Dingle, "Luminescent Transitions Associated With Divalent Copper Impurities and the Green Emission from Semiconducting Zinc Oxide", Phys. Rev. Lett. **23**, 579 (1969).

30. S. Monticone, R. Tufeu, and A. V. Kanaev, "Complex Nature of the UV and Visible Fluorescence of Colloidal ZnO Nanoparticles", J. Phys. Chem. B **102**, 2854 (1998).

31. A. Janotti and C.G. V. de Walle, "Native point defects in ZnO", Phys. Rev. B **76**, 165 202 (2007).

32. A. Azarov, A. Galeckas, E. Wendler, J. Ellingsen, E. Monakhov, and B. G. Svensson, "Normal and reverse defect annealing in ion implanted II-VI oxide semiconductors", J. Appl. Phys. **122**, 115701 (2017).

33. B. K. Meyer, H. Alves, D. M. Hofmann, W. Kriegseis, D. Forster, F. Bertram, J. Christen, A. Hoffmann, M. Straßburg, M. Dworzak, U. Haboeck, and A. V. Rodina, "Bound exciton and donor-acceptor pair recombination in ZnO", Phys. Stat. Sol. B **241**, 231 (2004).

34. M. Schirra, R. Schneider, A. Reiser, G. M. Prinz, M. Feneberg, J. Biskupek, U. Kaiser, C. E. Krill, K. Thonke, and R. Sauer, "Stacking fault related 3.31-eV luminescence at 130-meV acceptors in zinc oxide", Phys. Rev. B **77**, 125215 (2008).

35. C. H. Ahn, Y. Y. Kim, D. C. Kim, S. K Mohanta, and H. K. Cho, "A comparative analysis of deep level emission in ZnO layers deposited by various methods", J. Appl. Phys. **105**, 013502 (2009).

36. B. Cao, W. Cai, and H. Zeng, "Temperature-dependent shifts of three emission bands for ZnO nanoneedle arrays", Appl. Phys. Lett. **88**, 161101 (2006).

37. X. L. Wu, G. G. Siu, C. L. Fu, and H. C. Ong, "Photoluminescence and cathodoluminescence studies of stoichiometric and oxygen-deficient ZnO films", Appl. Phys. Lett., **78**, 2285 (2001).

38. S. H. Jeong, B. S. Kim, and B. T. Lee, "Photoluminescence dependence of ZnO films grown on Si(100) by radio-frequency magnetron sputtering on the growth ambient", Appl. Phys. Lett. **82**, 2625 (2003).

39. S. Mahamuni, K. Borgohain, B. S. Bendre, V. J. Leppert, and S. H. Risbud, "Spectroscopic and structural characterization of electrochemically grown ZnO quantum dots", J. Appl. Phys., **85**, 2861 (1999).

40. L. Xu, S. P. Lau, J. S. Chen, G. Y. Chen, and B. K. Tay, "Polycrystalline ZnO thin films on Si (100) deposited by filtered cathodic vacuum arc", J. Cryst. Growth, **223**, 201 (2001).

41. A. Azarov, B. L. Aarseth, L. Vines, A. Hallén, E. Monakhov, and A. Kuznetsov, "Defect annealing kinetics in ZnO implanted with Zn substituting elements: Zn interstitials and Li redistribution", J. Appl. Phys. **125**, 075703 (2019).

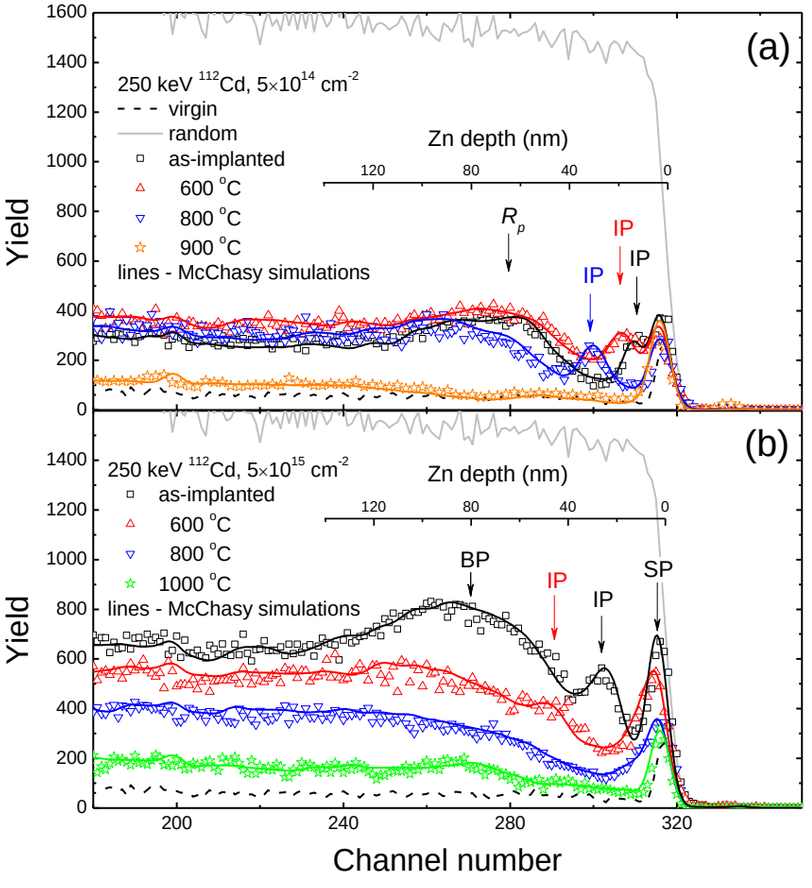

FIG. 1. RBS/C spectra of ZnO implanted with 250 keV Cd ions to low (a) and high (b) ion doses before and after annealing as indicated in the legends. The channeling spectra simulated with McChasy code are shown by the solid lines. The channeling spectrum of unprocessed (virgin) sample is shown for comparison by the dashed line. The positions of intermediate, bulk and surface damage peaks labeled as IP, BP and SP, respectively, are indicated by the arrows. The RBS spectrum from a randomly oriented sample is also shown. The R_p position is indicated in the panel (a).

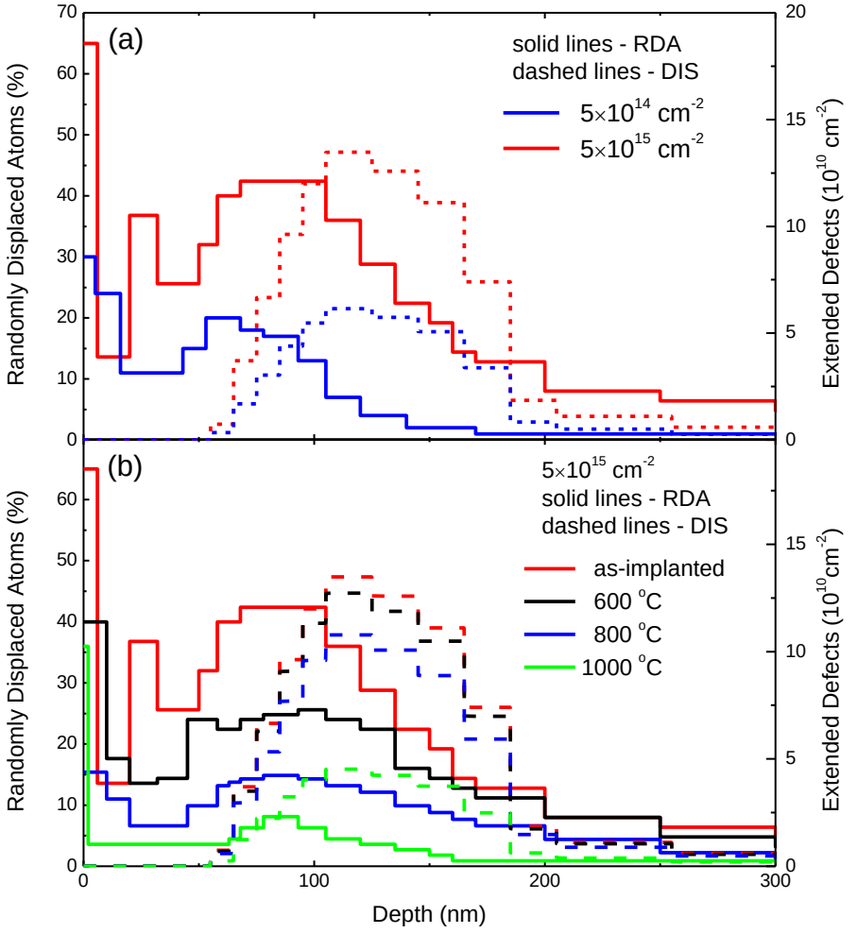

FIG. 2. Depth profiles of randomly displaced atoms (RDA, solid lines, left-hand scale) and extended defects (DIS, dashed lines, right-hand scale) obtained with McChasy code simulations for (a) as-implanted samples with Cd ions to low and high Cd doses, and (b) high dose implanted samples before and after different anneals as indicated in the legend.

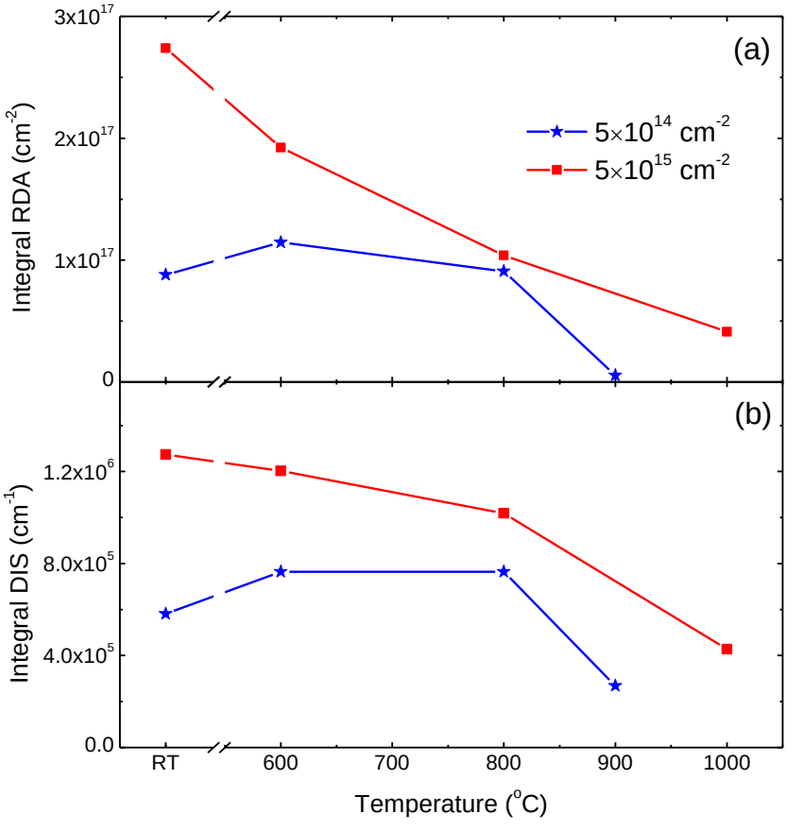

FIG. 3. Integral amounts of (a) RDA and (b) DIS defects as a function of annealing temperature for ZnO implanted with Cd ions to low and high ion doses as indicated in the legend.

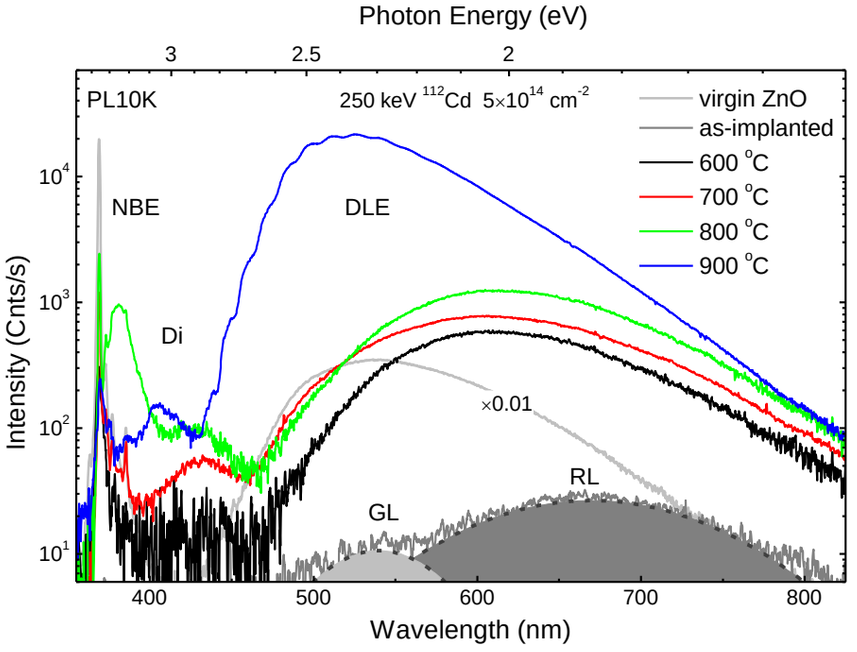

FIG. 4. PL spectra taken at 10K of ZnO implanted with 250 keV Cd ions to the ion dose of 5×10^{14} cm^{-2} before and after different anneals as indicated in the legend. The main spectral constituents are marked by NBE, DLE and Di labels; Gaussian (shaded areas) curves highlight the RL and GL bands within the multi-component structure of DLE. Note that intensity of the reference spectrum of virgin ZnO is scaled down by a factor of 0.01.

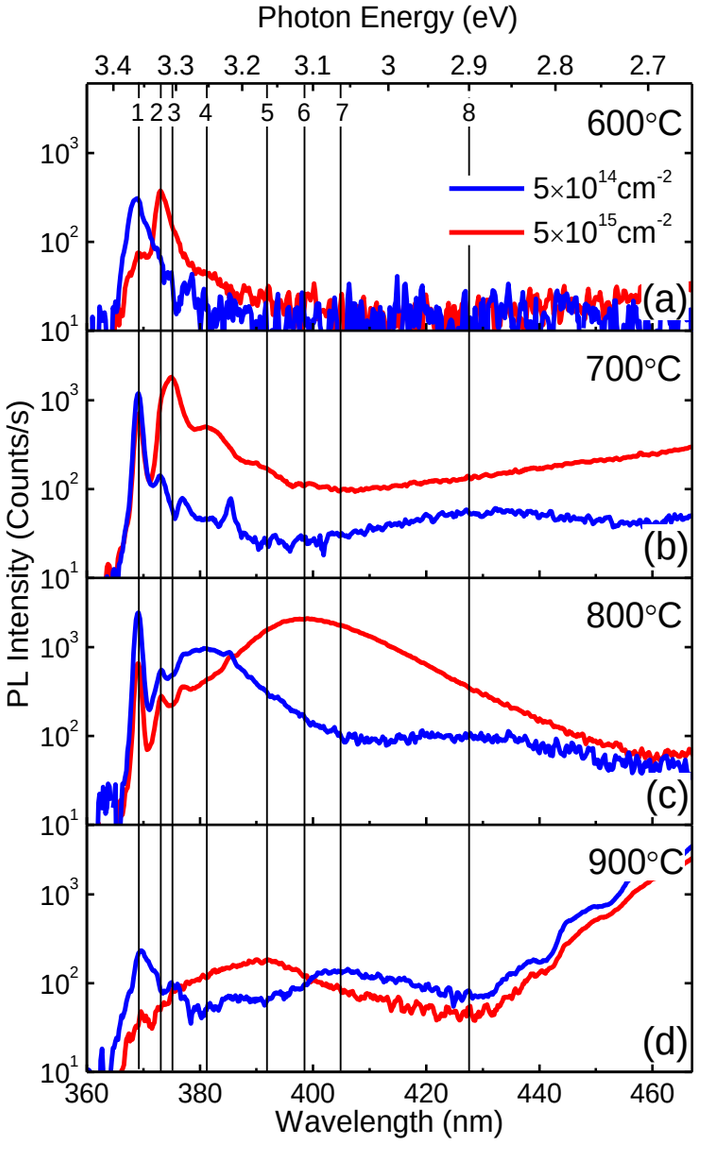

FIG. 5. Developments in the NBE and Di regions of PL spectra at 10K of ZnO samples implanted with 250 keV Cd ions to low (5×10^{14} cm^{-2}) and high (5×10^{15} cm^{-2}) doses after 600°C, 700°C, 800°C and 900°C anneals (panels a-d, respectively). Vertical drop lines (1-8) indicate the key emission components discussed in the text.

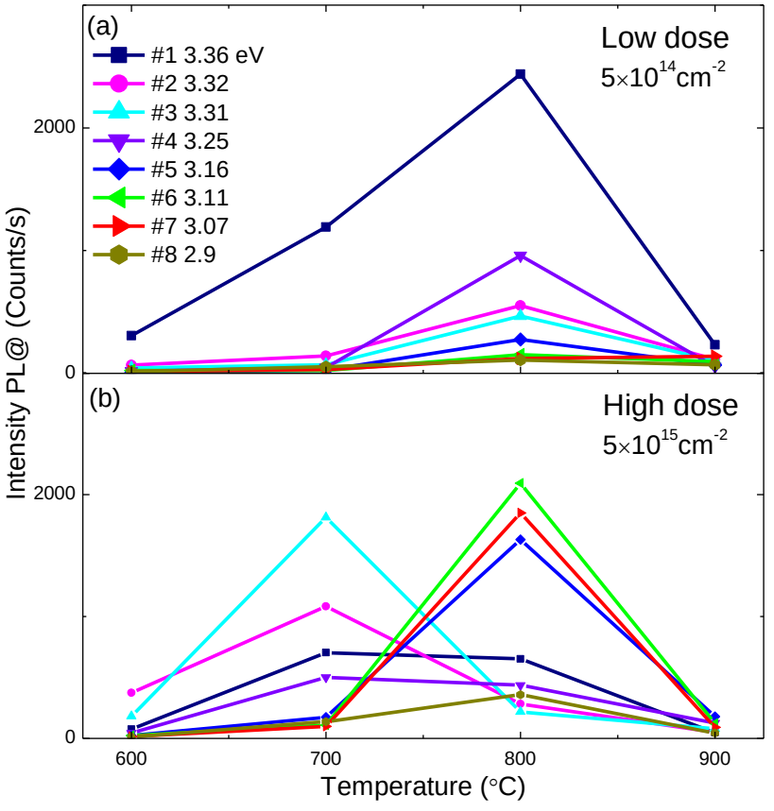

FIG. 6. PL intensities of the key spectral components designated in Fig. 5 as a function of annealing temperature.

Journal of Applied Physics

AIP Publishing

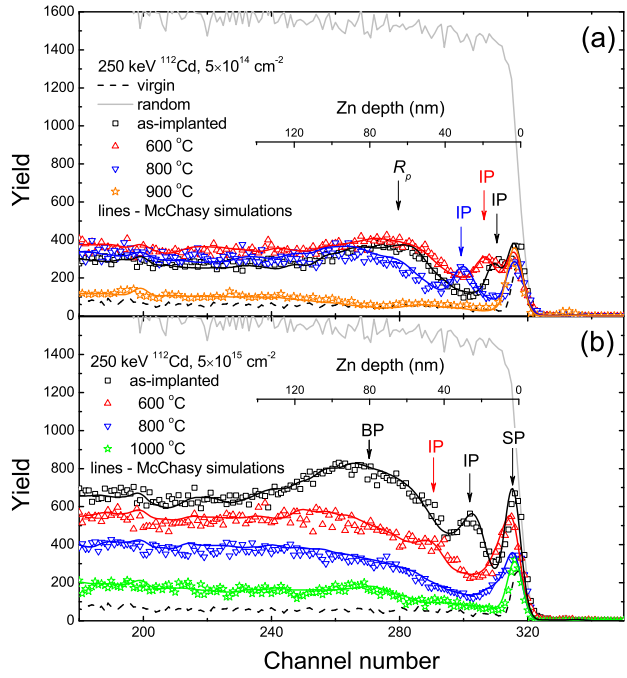

AIP Publishing

Journal of Applied Physics

ACCEPTED MANUSCRIPT

PLEASE CITE THIS ARTICLE AS DOI: 10.1063/1.5134011

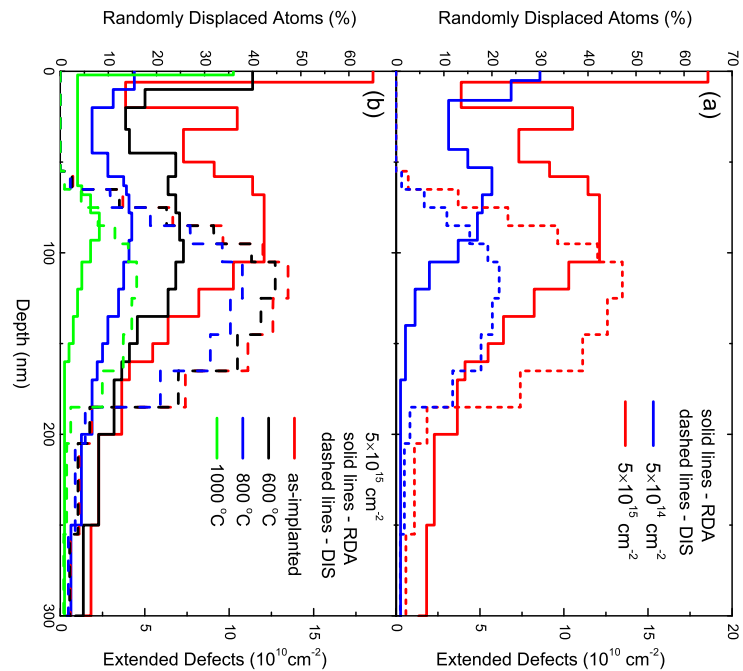

PLEASE CITE THIS ARTICLE AS DOI: 10.1063/1.5134011

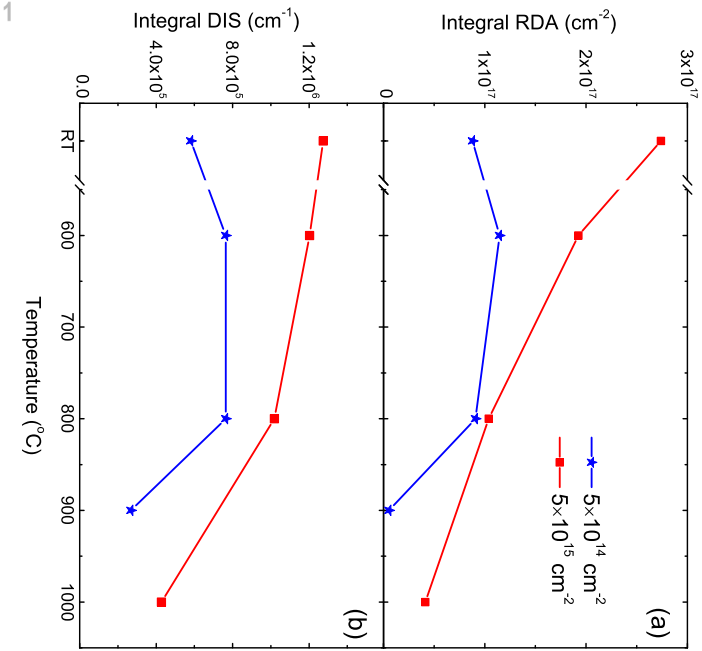

AIP Publishing

Journal of Applied Physics

PLEASE CITE THIS ARTICLE AS DOI: 10.1063/1.5134011

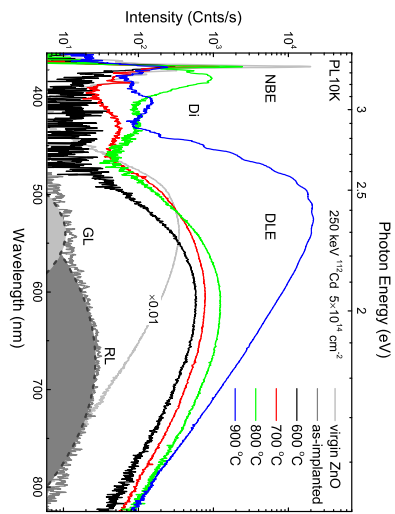

AIP Publishing

Journal of Applied Physics

ACCEPTED MANUSCRIPT

PLEASE CITE THIS ARTICLE AS DOI: 10.1063/1.5134011

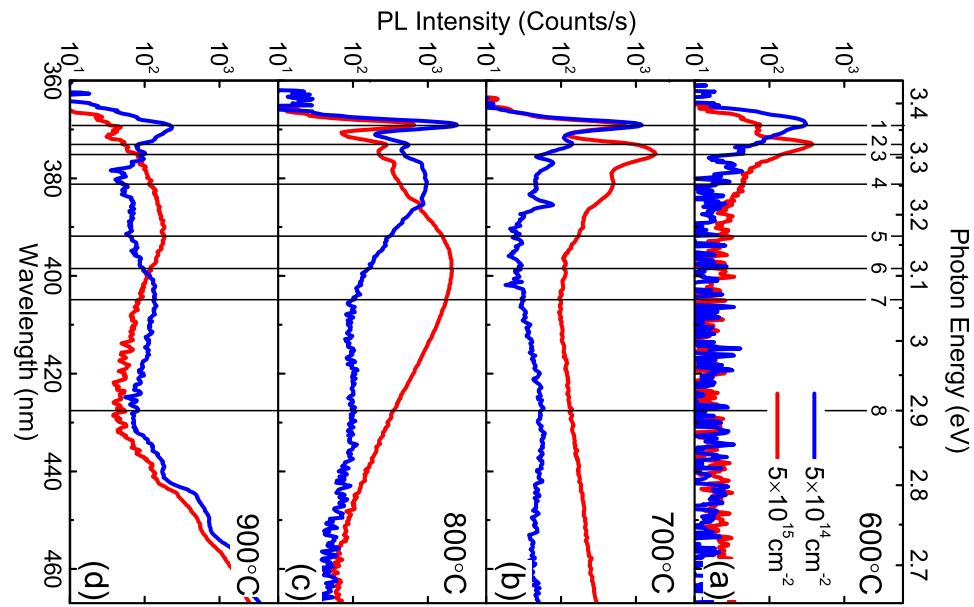

Journal of Applied Physics

PLEASE CITE THIS ARTICLE AS DOI: 10.1063/1.5134011